

Quality Assessment Techniques Applied to Surface Radial Velocity Maps Obtained from High-Frequency Radars

SUNG YONG KIM

Department of Mechanical Engineering, School of Mechanical and Aerospace Engineering, Korea Advanced Institute of Science and Technology, Daejeon, South Korea

(Manuscript received 13 November 2014, in final form 4 May 2015)

ABSTRACT

This paper presents examples of the data quality assessment of surface radial velocity maps obtained from shore-based single and multiple high-frequency radars (HFRs) using statistical and dynamical approaches in a hindcast mode. Since a single radial velocity map contains partial information regarding a true current field, archived radial velocity data embed geophysical signals, such as tides, wind stress, and near-inertial and low-frequency variance. The spatial consistency of the geophysical signals and their dynamic relationships with driving forces are used to conduct the quality assurance and quality control of radial velocity data. For instance, spatial coherence, tidal amplitudes and phases, and wind-radial transfer functions are used to identify a spurious range and azimuthal bin. The uncertainty and signal-to-noise ratio of radial data are estimated with the standard deviation and cross correlation of paired radials sampled at nearby grid points that belong to two different radars. This review paper can benefit HFR users and operators and those who are interested in analyzing HFR-derived surface radial velocity data.

1. Introduction

Surface current measurement using a shore-based high-frequency radar (HFR) is based on the interpretation of Bragg-scattered returns of transmitted radio signals. Bragg signals are backscattered in phase with the transmitted signals, whose wavelengths are twice those of ocean surface gravity waves (e.g., [Stewart and Joy 1974](#); [Crombie 1955](#); [Barrick et al. 1977](#); [Paduan and Washburn 2013](#)). A radial velocity map, obtained from multiple steps of the spectral analysis of return signals, consists of a set of radial velocities and bearing angles on a polar coordinate grid. The radial velocity is computed from the shifted amount of Bragg peaks in a Doppler spectrum, and the bearing angle is estimated using either direction finding or beamforming depending on the antenna's characteristics (e.g., [Schmidt 1986](#); [Teague et al. 2001](#)).

Since HFR-derived surface current observations resolve coastal surface circulation from the shoreline

(except for the surfzone) to $O(100)$ km offshore at a resolution of hours in time and kilometers in space, they have supported studies of submesoscale coastal circulation and the development of relevant environmental applications (e.g., [Shay et al. 1995](#); [Kim et al. 2011](#); [Paduan and Washburn 2013](#); [Essen et al. 1999](#)). For instance, scientific studies on submesoscale vortices and fronts (e.g., [Shay et al. 1998](#); [Chavanne et al. 2010b](#); [Kim 2010](#)) and practical applications for tracking pollutants and larvae and for assisting search and rescue missions (e.g., [Ullman et al. 2006](#); [Kaplan and Largier 2006](#); [Kim et al. 2009b](#); [Rogowski et al. 2015](#)) have been conducted. Moreover, large-scale coastal surface circulation, including alongshore variation in surface tidal currents and the signals of coastally trapped waves, has been explored with a network of HFRs off the U.S. West Coast (e.g., [Kim et al. 2011](#); [Bjorkstedt et al. 2010](#)).

However, as archived HFR-derived data are relatively abundant compared to data from other remote sensing and in situ observations, it has been difficult to handle and analyze them. Moreover, the importance of an integrated analysis of high-resolution coastal observations has been raised, including HFR-derived surface currents (e.g., [Kim et al. 2011](#)) and submesoscale sea surface heights obtained from satellite missions (e.g., [Fu and Ferrari 2008](#); [Uematsu](#)

Corresponding author address: Sung Yong Kim, Department of Mechanical Engineering, School of Mechanical and Aerospace Engineering, Korea Advanced Institute of Science and Technology, 291 Daehak-ro, Yuseong-gu, Daejeon 34141, South Korea.
E-mail: syongkim@kaist.ac.kr

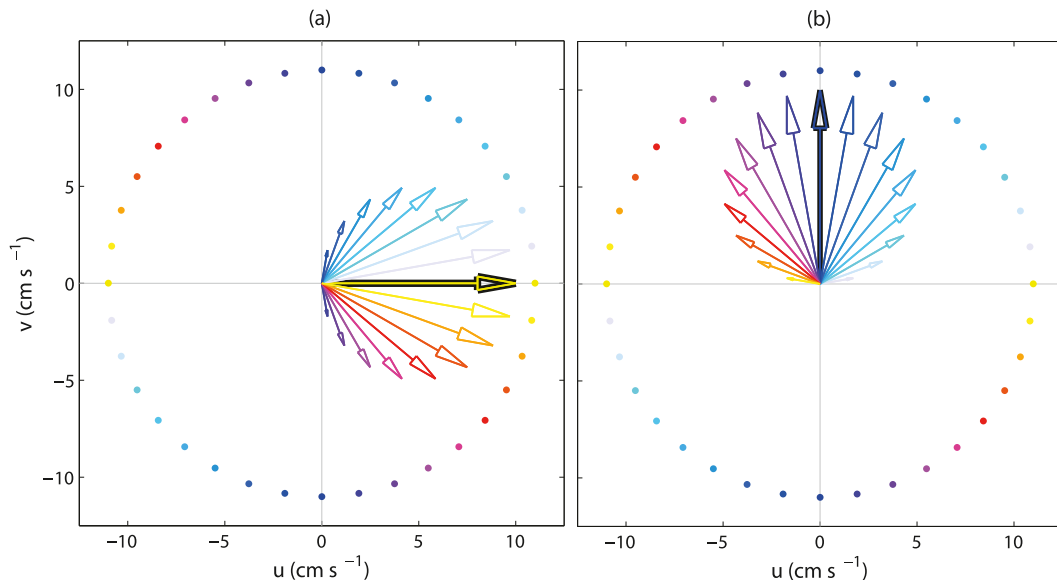


FIG. 1. Examples of radial velocities (colored arrows) when a vector current (black arrow) is projected onto a line connecting a colored grid point (location of an HFR) and the center where the vector current is sampled.

et al. 2013). Thus, the rudimentary quality assessment on those high-resolution data has been demanded, which can be aligned with enhanced awareness of building and sustaining regional coastal ocean observing programs (e.g., Malone and Cole 2000; Ocean.US 2002; Stokstad 2006). In this paper, detailed and technical descriptions of HFR data analysis are presented in terms of the quality assurance and quality control (QAQC) of radial velocity data based on the expected geophysical signals and dynamic relationships between driving forces and responses. This work will be beneficial and instructive not only for HFR operators and users within different levels of experience but also for those who work on the analysis of high-resolution geophysical data in time and space by providing systematic and practical guidelines. Although this paper can be incorporated into existing common practice, it is designed to encourage beginners to address HFR-derived data analysis easily and efficiently and to reduce the labor involved in researching techniques scattered among other references. For reference, comprehensive analyses of HFR-derived spectral raw data (prior to the radial data extraction) have been addressed elsewhere (e.g., Kirincich et al. 2012; Flores-Vidal et al. 2013).

The paper is divided into three sections. The temporal and spatial data availability of radials are defined for a systematic organization and analysis of archived radial velocity data (section 2). Geophysical signals in radial velocity data (section 3a) are used to examine spatial consistency, such as spatial coherence in specific frequency bands (section 3b), maps of tidal amplitudes and phases (section 3c), and wind-radial transfer function analysis

(section 3d). The uncertainty and signal-to-noise ratio (SNR) of radials are also discussed (section 3e). Finally, the proposed analysis and results are summarized (section 4).

2. An overview

a. Radial velocity data

A radial velocity (r) is a projected component of a vector current (u and v) with respect to the bearing angle (θ) of the radar:

$$r = u \cos \theta + v \sin \theta. \quad (1)$$

Figure 1 illustrates the reported radial velocities when a true vector current (black arrows) is measured by a radar located at colored dots. The radial velocities are scalar components projected onto a line connecting a colored grid point and a grid point where the vector current is sampled (examples of the radial velocity map are shown in Figs. 2c and 4a).

A radial grid consists of range and azimuthal bins on a polar coordinate (Fig. 2a). The range spacing depends on the operating and sweeping frequencies, and the azimuthal spacing varies from 1° to 5° . Figure 2a shows examples of a radial grid having two types of grid spacing, namely, $1.5 \text{ km} \times 1^\circ$ (green dots) and $4.5 \text{ km} \times 5^\circ$ (blue or red crosses). A single radial velocity is reported as a scalar value spatially averaged over a polar grid patch, which is the smallest unit in the polar coordinate grid. More details on the spatial spacing of the radial grid and bin averaging of radials will be discussed in section 3c.

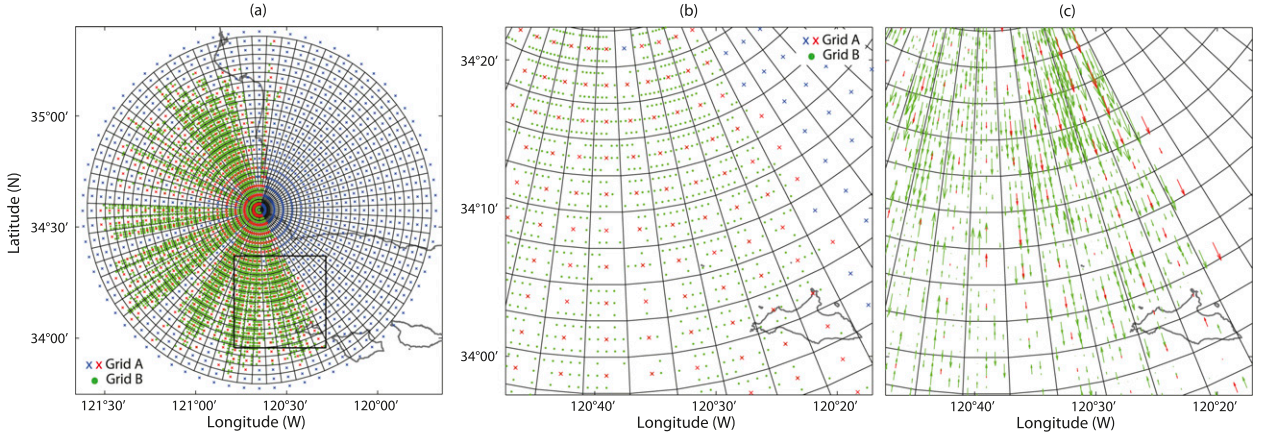


FIG. 2. (a) An example of HFR radial grids. A radial grid at ARG1 (San Luis Obispo) shows two different grid spacings of $1.5 \text{ km} \times 1^\circ$ (grid A; green dots) and $4.5 \text{ km} \times 5^\circ$ (grid B; blue or red crosses). Grid B is a bin-averaged radial grid of grid A. Bin-averaged radials are marked with red dots (no bin-averaged radials are denoted with blue dots). (b),(c) A magnified view of the radial grid and (bin averaged) radial velocities in the black box in (a).

In this paper, the radial velocity data are mainly obtained from compact array HFR systems off California (e.g., San Diego and San Luis Obispo) and Oregon (e.g., Manhattan Beach) in the United States, and Yeosu (e.g., Yeosu Bay) in South Korea (see Table 1 for more details). Since the examples presented in the paper are chosen to highlight the proposed techniques, the radial data had to be taken from different regional locations. However, the proposed techniques are applicable to any radial velocity data at the discretion of the user. Additionally, as a compact array system (e.g., SeaSonde) reports two types of radials—radials processed with ideal and measured beam patterns—two sets of radials can be considered simultaneously or separately in the following analyses.

b. Data availability

As a first step in the hindcast evaluation of archived radial velocity maps (Fig. 3a), the temporal data

availability [d_i ; Eq. (2)] of radials is defined as the ratio of the number of total radial solutions to their maximum number at each time point (Figs. 3b and 3c):

$$d_i(t) = \frac{\sum_m \sum_\theta N(m, \theta, t)}{\max \left| \sum_m \sum_\theta N(m, \theta, t) \right|}, \quad (2)$$

where $N(m, \theta, t)$ is a binary expression (e.g., zero for missing data and one for observed data) of radial velocity maps as a function of space (m for a range bin and θ for an azimuthal angle) and time (t).

The spatial data availability [d_s ; Eq. (3)] of radials is defined as the ratio of the number of radial solutions at each range and azimuthal bin to the number of time records (E_t) within a selected time period (e.g., $E_t = 17\,544$ in the case of hourly records over a period of 2 years) (Figs. 3d and 3e):

TABLE 1. Detailed specifications of high-frequency radars participating in the hindcast analysis are listed with station identification (ID; region), operating frequency (f_o ; MHz), and transmitted bandwidth (f_b ; kHz) of the HFRs, and the range spacing (Δs ; km), azimuthal spacing ($\Delta\theta$; $^\circ$), time interval (Δt ; h), and averaging time window (Δt_w ; h) of the radial velocity maps. Stations are listed in the order presented in the text.

Station ID (region)	f_o	f_b	Δs	$\Delta\theta$	Δt	Δt_w
ARG1 (San Luis Obispo, CA)	13.499	99.26	1.510	1	1.00	1.25
SDBP (San Diego, CA)	25.799	101.10	1.484	5	1.00	1.25
NAM4 (Yeosu)	25.800	199.58	0.751	1	0.50	1.25
MAN1 (Manhattan Beach, OR)	4.785	25.73	5.829	5	1.00	3.00
SDCI (San Diego, CA)	24.730	101.10	1.484	5	1.00	1.25
SDPL (San Diego, CA)	24.500	101.10	1.484	5	1.50	1.25
HYIL (Yeosu)	24.525	199.58	0.751	1	0.50	1.25
NHSP (Yeosu)	42.400	300.00	0.500	1	0.50	1.25
ODNG (Yeosu)	43.500	300.00	0.500	1	0.50	1.25

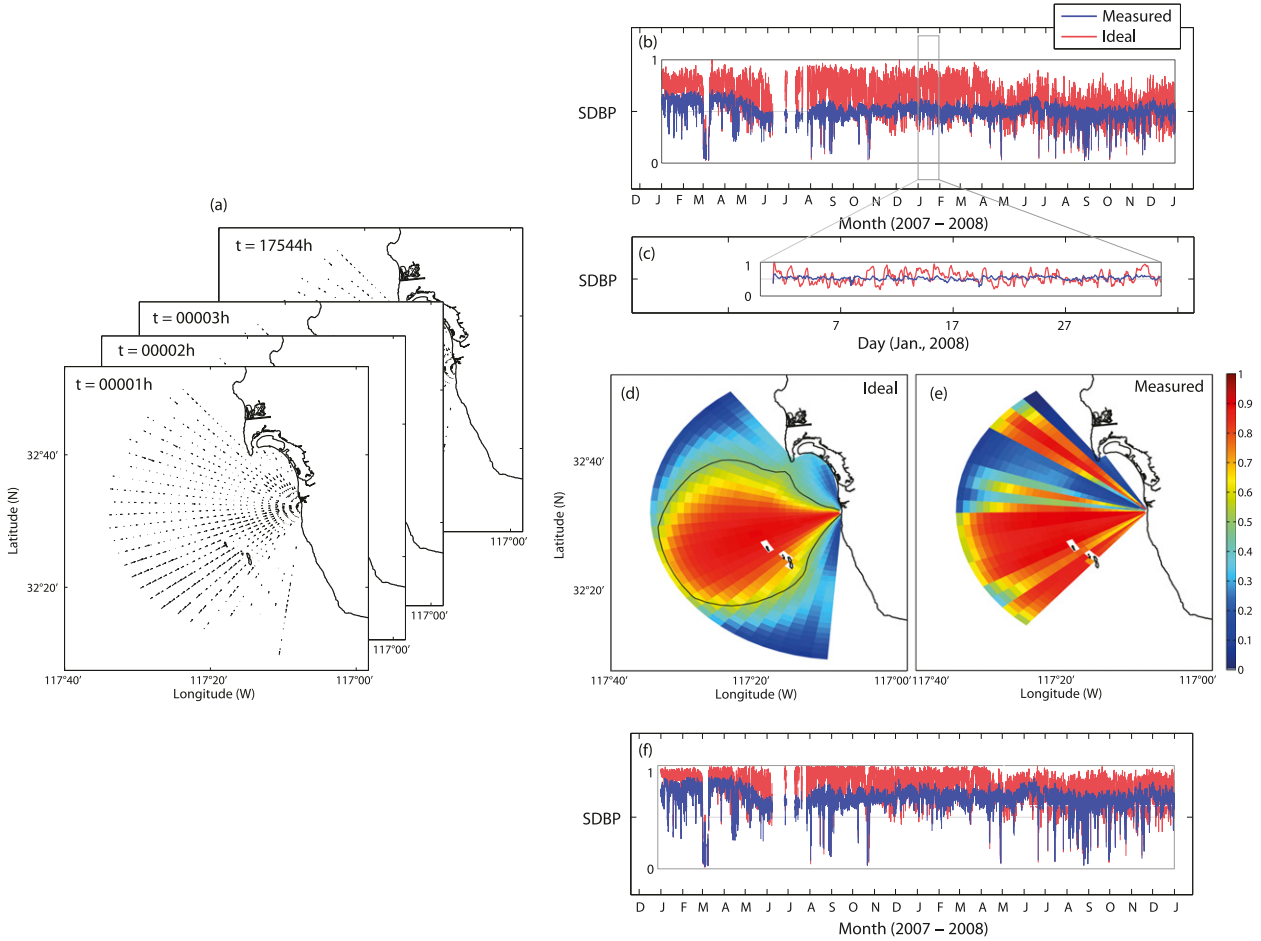


FIG. 3. An example of the initial treatment of radial velocity data in a hindcast mode. The total number of radial solutions and the number of radial solutions at individual azimuthal and range bins at SDBP (San Diego) for a period of 2 years (2007–08) are used to report the temporal and spatial data availability. (a) Examples of radial velocity maps. (b),(c) Temporal data availability [d_t ; Eq. (2)] of radials estimated by ideal (red) and measured (blue) beam patterns for a period of 2 years and 1 month (January 2008). Temporal data availability is reported as zero for no solutions and one for the maximum number of solutions within the time period. (d),(e) Spatial data availability [d_s ; Eq. (3)] of radials estimated by ideal and measured beam patterns, respectively. A black contour in (d) indicates an effective spatial coverage with more than 50% spatial data availability (e.g., 454 grid points). (f) Effective temporal data availability [d_g ; Eq. (4)] normalized by the number of radials within 50% spatial data availability.

$$d_s(m, \theta) = \frac{1}{E_t} \sum_t N(m, \theta, t). \quad (3)$$

The effective temporal data availability [d_g ; Eq. (4)] of radials is defined by the number of effective radial grid points (E_g), which are chosen as an area (m_g, θ_g) with more than α of spatial data availability ($d_s \geq \alpha$, $0 < \alpha \leq 1$) (Fig. 3f):

$$d_g(t; \alpha) = \frac{1}{E_g} \sum_{m_g} \sum_{\theta_g} N(m, \theta, t), \quad (4)$$

where α is a threshold value of the spatial data availability of radials over a given time period.

A radial grid at SDBP (San Diego) consists of 72 azimuthal bins and 40 range bins (Fig. 3a). Hourly radial velocity maps over a period of 2 years (2007–08) are counted as a function of time and space ($E_t = 17544$). The temporal data availability of ideal (blue) and measured (red) radials (Figs. 3b and 3c) can be used to identify significant downtime and its temporal periodicity. The spatial data availability of ideal (Fig. 3d) and measured (Fig. 3e) radials can diagnose a spatial bias. The effective temporal data availability is defined using an effective spatial coverage of radials [$\alpha = 0.5$ in Eq. (4)] (Fig. 3f). Note that radial grid points on land and islands can be excluded from the shorelines and boundaries of islands.

A clear definition of the temporal and spatial data availability is useful for communications within the

HFR community and for introducing beginners to the organization of archived radial velocity data.

c. Range spacing and azimuthal spacing

In the context of sampling of surface circulation, an optimal spacing of a radial velocity map in the azimuthal and range directions can be determined by the wavenumber energy spectra of radials (Fig. 4). Figure 4a shows a snapshot of radial velocity maps reported at NAM4 (Yeosu Bay), which has 1° azimuthal spacing and 0.75-km range spacing. The energy spectra of hourly radial velocities along a range bin (red) and an azimuthal angle (blue) are averaged over a period of 5 months (March–July 2011), as shown in Figs. 4b and 4c, respectively.

An optimal sampling spacing can be determined by a wavenumber whose variance is saturated because nearly flat variance beyond a specific wavenumber indicates that there is no new information below that length scale. Figure 4b shows that the saturation of variance or a floor level starts near 0.1 cycles per degree (cpdg), which is equal to the Nyquist wavenumber of data sampled with 5° spacing. Thus, the optimal azimuthal spacing for this site can be higher than 5° . Conversely, an averaged energy spectrum along the azimuthal bin does not show saturation of signals. Thus, an original range spacing of 0.75 km for this site is a reasonable value (Fig. 4c). Moreover, the energy spectra of radial velocities along other azimuthal and range bins show consistent results.

d. Bin averaging of radials

In combining multiple radial velocity maps with different spatial spacing into a vector current map, high-resolution (spacing) radial velocity maps may generate a spatial bias in a mapped vector current field, which is related neither to the beam pattern nor intrinsic radar issues (e.g., Kim et al. 2011). Thus, radial velocity maps may require bin averaging to make their spatial spacing comparable (e.g., 3–5-km range and 5° azimuthal spacing). Figure 2a shows examples of radials reported on a grid of 1° azimuthal spacing and 1.5-km range spacing (green dots) and bin-averaged radials on a grid of 5° azimuthal spacing and 4.5-km range spacing (blue and red crosses) (Figs. 2b and 2c are magnified from Fig. 2a). The radial velocities before and after bin averaging are shown in Fig. 2c. In this bin averaging of radials, a threshold number of radials can be applied to provide statistical significance for spatially averaged radials. Note that methods combining multiple radial velocity maps into a vector current have been discussed elsewhere (e.g., Lipa and Barrick 1983; Kim et al. 2008).

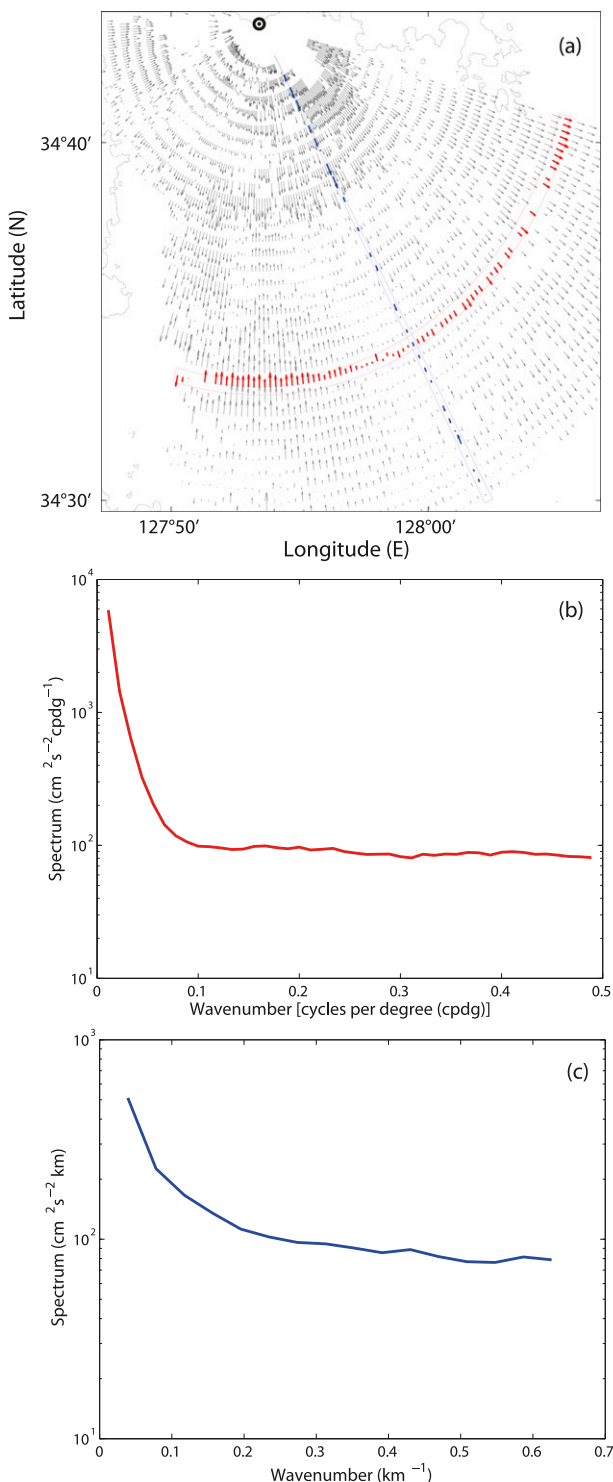


FIG. 4. (a) An hourly radial velocity map at NAM4 (Yeosu Bay) 1300 UTC 10 Mar 2011. Radial velocities along a range bin (red) and an azimuthal bin (blue) are chosen to estimate the wavenumber spectra in (b) and (c). Wavenumber spectra are averaged over a period of 5 months (March–July 2011). (b) An averaged wavenumber spectrum of radial velocities along a range bin. (c) An averaged wavenumber spectrum of radial velocities along an azimuthal bin.

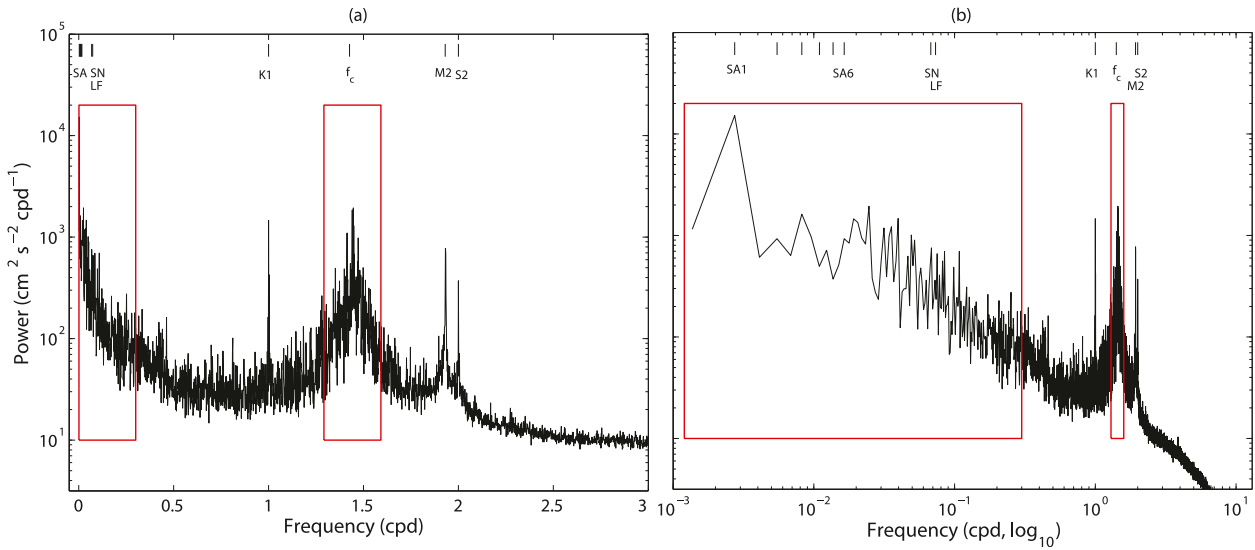


FIG. 5. A spatially averaged frequency-domain energy spectrum of hourly radial velocities at MAN1 (Manhattan Beach) over 225 grid points with more than 80% temporal data availability for a period of 2 years (2007–08). Barotropic tides (K_1 , M_2 , and S_2), spring–neap (SN; 14.765 days) and lunar fortnightly (LF; 13.661 days) tides, and seasonal cycle and its five harmonics (SA_1 , SA_2 , ..., SA_6) are marked. The scales of the horizontal axis are (a) linear and (b) \log_{10} . Two frequency bands of low frequency ($0 < \sigma \leq 0.3$ cpd) and near-inertial frequency ($|\sigma - f_c| \leq 0.15$ cpd) are marked with red boxes in (a),(b), respectively, which have been used in spatial coherence estimates in Fig. 6.

3. Data analysis

a. Geophysical signals

Since a single radial velocity map contains partial information of a true vector current field [Eq. (1)], it includes geophysical signals of ageostrophic and geostrophic currents, barotropic and baroclinic tidal currents, and near-inertial currents (e.g., Kim et al. 2010a, 2011). An averaged energy spectrum of hourly radial velocities at 225 grid points with more than 80% spatial data availability [$\alpha = 0.8$ in Eq. (4)] at MAN1 over a period of 2 years (2007–08) is shown on the same frequency axes with two different scales—a linear scale (Fig. 5a) and a \log_{10} scale (Fig. 5b)—to highlight the variance in the subdiurnal and superdiurnal frequency bands, respectively. Note that the representing inertial frequency (f_c) in this region is 1.47 cycles per day (cpd). Dominant variance appears in a low-frequency band ($\sigma \leq 0.3$ cpd) and in a near-inertial frequency band ($|\sigma - f_c| \leq 0.15$ cpd; red boxes in Fig. 5), and at diurnal (S_1 and K_1) and semi-diurnal (M_2 and S_2) frequencies. The spatial structure of dominant variance can be used to identify spurious radial data (see sections 3b–3d for more details).

The geophysical signals of radial velocity data can be evaluated with those in independent observations of currents (e.g., ADCP, current meter, and altimeter data). Additionally, maps with near-inertial variance, tidal amplitudes and phases, and low-frequency variance of radial

velocities can reveal where and when the signals are inconsistent. Although radial velocities are sampled on a polar coordinate grid, these geophysical signal maps have a unique spatial structure in a physical space. Thus, discontinuously enhanced and biased features along an azimuthal bin or a range bin can be flagged as nonphysical components and instrumental noise. The following analysis provides more detailed examples.

b. Spatial coherence

The variability of ocean currents is represented with unique decorrelation scales depending on driving forces and oceanic responses in a frequency band of interest (e.g., Dickey et al. 2006; Kim et al. 2010a). Spatial coherence can be regarded as the spatial correlation within a specific frequency band (e.g., Emery and Thomson 1997; Kim et al. 2010b):

$$c(\Delta \mathbf{x}, \bar{\sigma}) = \frac{\langle \hat{r}(\mathbf{x}, \bar{\sigma}) \hat{r}^\dagger(\mathbf{x} + \Delta \mathbf{x}, \bar{\sigma}) \rangle}{\sqrt{\langle |\hat{r}(\mathbf{x}, \bar{\sigma})|^2 \rangle} \sqrt{\langle |\hat{r}(\mathbf{x} + \Delta \mathbf{x}, \bar{\sigma})|^2 \rangle}}, \quad (5)$$

where \hat{r} is the Fourier coefficients of radial velocity time series. The angle brackets ($\langle \cdot \rangle$) and the dagger (†) indicate an expectation over a given frequency band ($\bar{\sigma}$) and complex conjugate, respectively. Negative (positive) phases indicate that a referenced physical variable at \mathbf{x} leads (follows) a targeted physical variable at $\mathbf{x} + \Delta \mathbf{x}$.

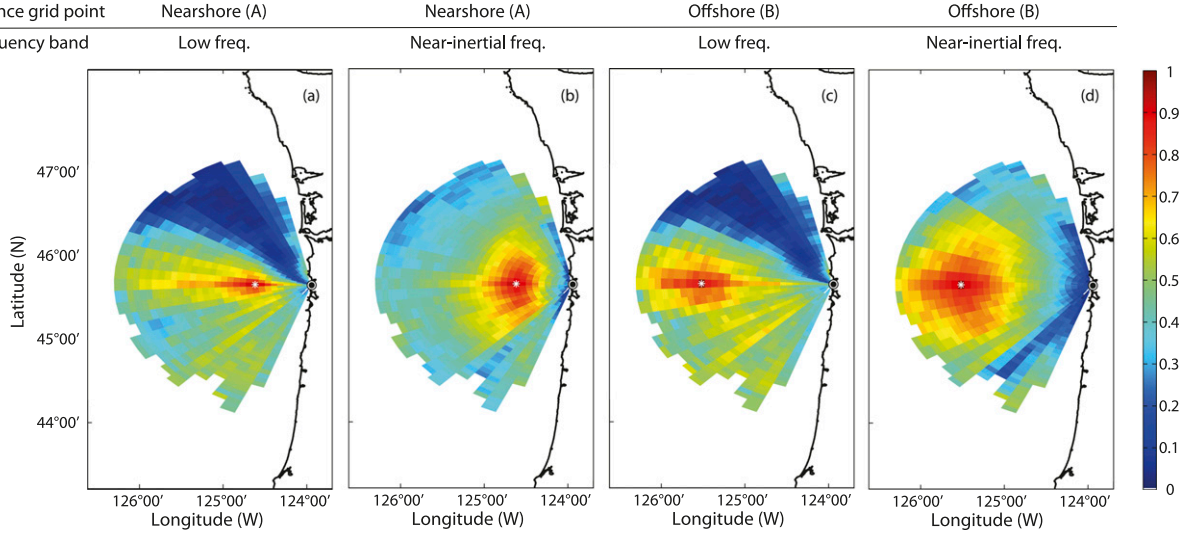


FIG. 6. Spatial coherence of hourly radial velocities between a reference radial grid point (white star) and other radial grid points in two frequency bands. (a),(c) Low-frequency band ($0 < \sigma \leq 0.3$ cpd). (b),(d): Clockwise near-inertial frequency band ($|\sigma - f_c| \leq 0.15$ cpd, where f_c is the local Coriolis frequency at the reference grid point). (a),(b) A nearshore gridpoint A. (c),(d): An offshore gridpoint B.

Hourly radial velocity maps at MAN1 over 225 grid points for a period of 2 years (2007–08) are analyzed to estimate the spatial coherence of radials between a reference grid point (a white star) and other grid points in a low-frequency band ($0 < \sigma \leq 0.3$ cpd) and near-inertial frequency band ($|\sigma - f_c| \leq 0.15$ cpd, where f_c is the local Coriolis frequency at the reference grid point) (Fig. 6). The expected length scales of surface currents in these frequency bands are $O(100)$ km (e.g., Picaut et al. 1990; Kim and Kosro 2013; Johnson 2008), which can be used to discern the spatial bias in the azimuthal and range directions. Moreover, the spatial coherence can vary with the location of the reference, particularly depending on the distance from shoreline. Thus, the spatial coherence at the nearshore and offshore reference grid points is used to evaluate how well the radial velocity data capture the spatial structure of coastal circulation reflecting coastal boundary effects (Figs. 6a and 6b; Figs. 6c and 6d). A spatially narrow coherence in the azimuthal direction (Fig. 6a), an abruptly reduced spatial coherence (Figs. 6a and 6c), and a discontinuously enhanced coherence along two more azimuthal bins (Fig. 6c) can be flagged as outliers.

Spatial inconsistency may result from unfavorable physical environments around the radar system (e.g., interference due to metal structures and landforms), biased or uncalibrated radar beam patterns (section 3f), and footprints of geophysical forces. For instance, the temporal data availability of radials in tide-dominant areas can exhibit dependency on the periodicity of local tides, and the wind direction and fetch can affect the number of radial

solutions due to changes in the performance of backscattering associated with the steepness of surface waves (e.g., Mao and Heron 2008). Note that an evaluation based on spatial coherence requires a sufficient number of realizations to capture the variability of interest.

c. Tide-coherent structures

Spatial consistency can be examined with maps of radial velocities at a specific frequency, such as maps of tidal amplitudes and phases. To compare phases at individual radar sites in a consistent manner, the phase should be adjusted with a relative angle to a reference site because the phases of radials include bearing angles at each site. A radial velocity (r_A) reported at a radial grid point of site A is equal to the real part of a projected component of true vector currents ($\mathbf{u} = u + iv$) with respect to a bearing angle (θ_A):

$$r_A = u \cos \theta_A + v \sin \theta_A, \quad (6)$$

$$= \text{Re}[(u + iv)(\cos \theta_A - i \sin \theta_A)], \quad (7)$$

$$= \text{Re}[\mathbf{u} e^{-i\theta_A}]. \quad (8)$$

In the same way, a radial velocity (r_B) obtained at a radial grid point of site B is given as

$$r_B = u \cos \theta_B + v \sin \theta_B = \text{Re}[\mathbf{u} e^{-i\theta_B}]. \quad (9)$$

Thus, a phase adjustment allows us to compare tidal phase maps with a consistent convention based on the relationship of the Fourier coefficients of two radial velocities (\hat{r}_A and \hat{r}_B):

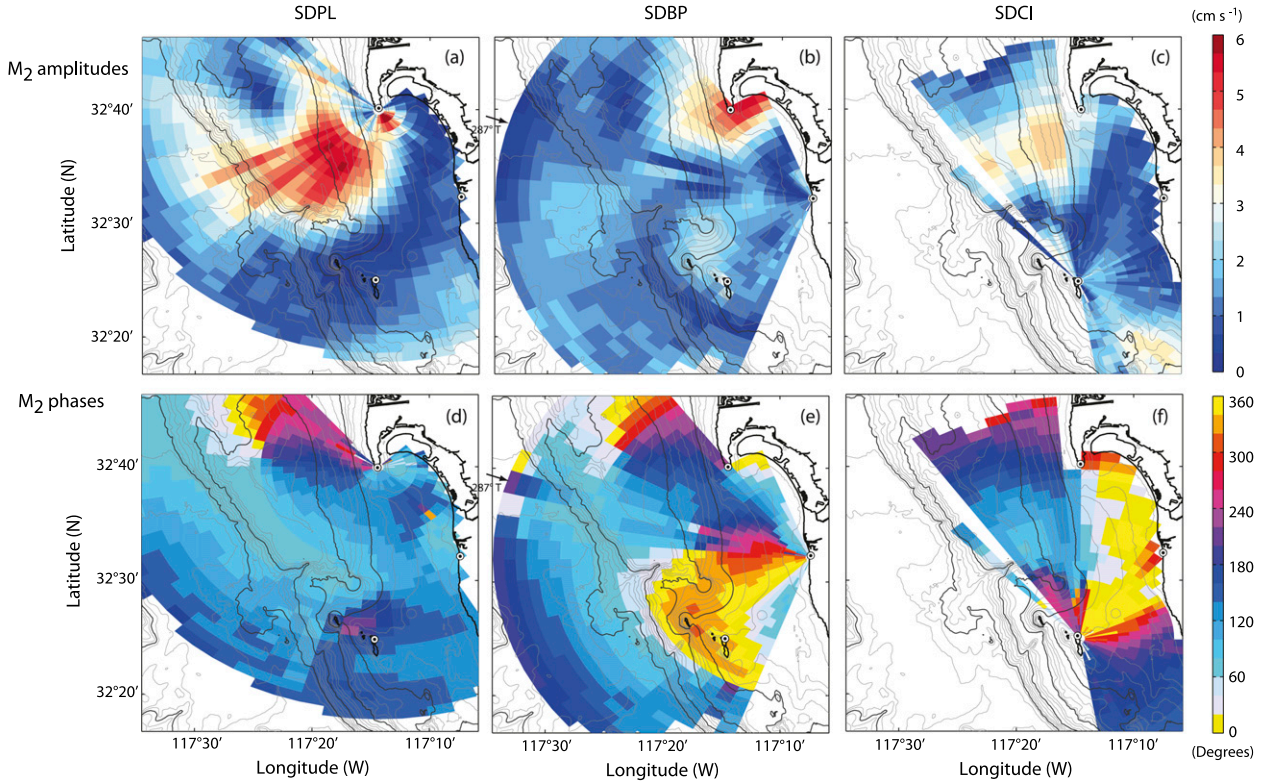


FIG. 7. Tidal amplitudes (cm s^{-1}) and phases (degrees) of hourly radial velocities at SDBP, SDPL, and SDCI (San Diego) at the M_2 frequency estimated using harmonic analysis. (a)–(c) Amplitudes (cm s^{-1}). (d)–(f) Phases ($^\circ$). The phases at SDBP and SDCI are adjusted with bearing angles relative to SDPL. (a),(d) SDPL. (b),(e) SDBP. (c),(f) SDCI. A black arrow in (b),(e) denotes an artifact at the 287° azimuthal bin (e.g., Fig. 10; Kim et al. 2010a).

$$\hat{r}_A = \hat{r}_B e^{-i(\theta_B - \theta_A)}. \quad (10)$$

The tidal amplitudes and phases of radials at SDBP, SDPL, and SDCI (San Diego) at the M_2 frequency are estimated with a least squares fit to the time series of radials over a period of 2 years (2003–05). Enhanced amplitudes (more than 3 cm s^{-1}) of M_2 tide-coherent radial velocities are commonly found onshore at Coronado Bank and at the mouth of San Diego Bay (Figs. 7a, 7b, and 7c). The phase maps in Figs. 7e and 7f are adjusted with respect to SDPL and show the onshore and offshore propagating features, which are consistent with the spatial pattern of phases of HFR-derived vector currents (e.g., Kim et al. 2010a), bottom slope, and a footprint of local synthetic aperture radar observations. Decorrelation length scales of surface currents at the M_2 frequency off southern San Diego are expected to be 20 km (e.g., Kim et al. 2010a), and a spurious azimuthal and range bin can be also identified in the amplitude and phase maps.

There are several coastal regions where M_2 internal tides have been identified by HFR observations, including Oregon (e.g., Kurapov et al. 2003); Bodega Bay

(e.g., Kaplan et al. 2005), off San Francisco Bay (e.g., Gough et al. 2010), and Monterey Bay (e.g., Paduan and Cook 1997; Rosenfeld et al. 2009) in California; and Hawaii (e.g., Zaron et al. 2009; Chavanne et al. 2010a).

d. Wind-coherent structures

Wind transfer function analysis provides a spectral relationship in the wind–current system using a statistical framework and is interpreted with coastal dynamics (e.g., Gonella 1972; Kim et al. 2009a, 2015). Using a linear parameterization between wind stress ($\hat{\tau}$) and radial velocity (\hat{r}) in the frequency domain (σ),

$$\hat{r}(\mathbf{x}, \sigma) = \mathbf{H}(\mathbf{x}, \sigma) \hat{\tau}(\mathbf{x}, \sigma), \quad (11)$$

the wind transfer function $[\mathbf{H}(\mathbf{x}, \sigma)]$ can be estimated with

$$\mathbf{H}(\mathbf{x}, \sigma) = \frac{\langle \hat{r}(\mathbf{x}, \sigma) \hat{\tau}^\dagger(\mathbf{x}, \sigma) \rangle}{\langle \hat{\tau}(\mathbf{x}, \sigma) \hat{\tau}^\dagger(\mathbf{x}, \sigma) \rangle + \langle \varepsilon \varepsilon^\dagger \rangle}, \quad (12)$$

where $\langle \varepsilon \varepsilon^\dagger \rangle$ is an error covariance of wind observations or a regularization matrix to adjust the overfitting and underfitting of the regression (e.g., Kim et al. 2009a).

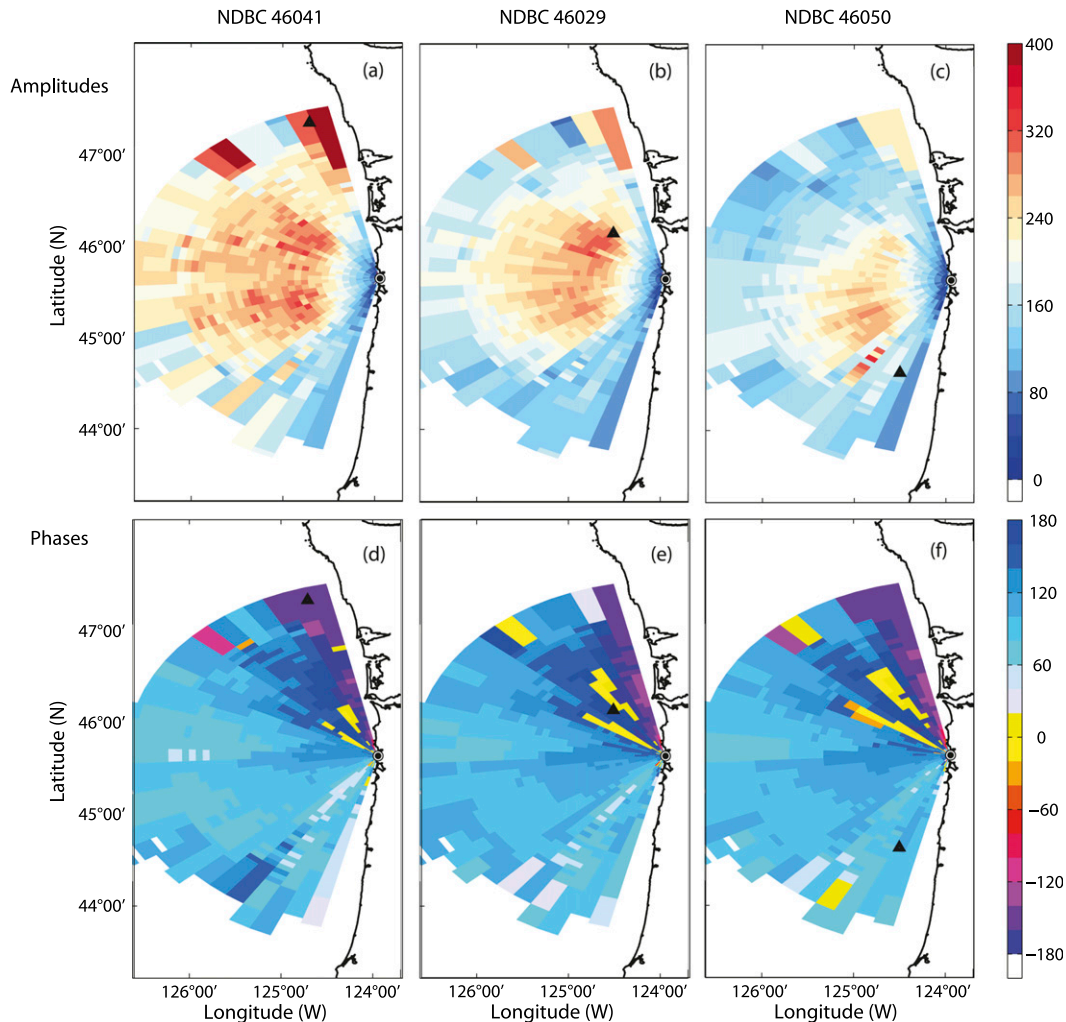


FIG. 8. Amplitudes [(a)–(c); kg⁻¹ m² s] and phases [(d)–(f); degrees] of wind transfer functions in a clockwise near-inertial frequency band ($|\sigma - f_c| \leq 0.15$ cpd). The wind transfer functions are estimated from detided radial velocity maps at MAN1 (Manhattan Beach) and wind stress at three individual NDBC buoys [(Cape Elizabeth (46041), Columbia River Bar (46029), and Stonewall Bank (46050)] for a period of 2 years (2007–08).

Wind-radial transfer functions are estimated from detided radial velocities at MAN1 and the wind stress at three individual NDBC buoys [Cape Elizabeth, Maine (46041); Columbia River Bar (46029); and Stonewall Bank, Oregon (46050)] over a period of 2 years (2007–08). The wind-radial transfer functions at specific frequencies or frequency bands with dominant variance (Fig. 5) can be used to evaluate relevant spatial structures. In this paper, amplitudes averaged over a clockwise near-inertial frequency band ($|\sigma - f_c| \leq 0.15$ cpd, where f_c is the Coriolis frequency where the radial velocity is reported) and phases at the clockwise inertial frequency are presented with three different locations of wind buoys (marked with black triangles) in Fig. 8. The amplitudes of the transfer functions appear enhanced in

the middle of the domain and differ by the locations of the wind buoys (Figs. 8a–8c). The spatial distribution of the phases and the range of their maximum and minimum are consistent for three wind buoys (Figs. 8d–8f). Several spotted radial patches (yellow and pink patches) are not consistent with a spatially increasing phase pattern from offshore to nearshore and can help us identify inconsistent azimuthal and range bins.

Figure 8 exhibits results from a single radar and three different wind buoys. When radials obtained from multiple radars are used, the phase of the transfer functions should be adjusted to interpret the results in a consistent manner (section 3c). This approach allows us to identify spatial inconsistencies using independent in situ observations (e.g., wind).

e. Uncertainty

As in section 3c, a pair of radial velocity time series reported from both a polar grid patch of a similar size and two different radars can provide an independent evaluation of an array of radars in a coastal region. For example, the standard deviation and cross correlation of radial pairs are used to estimate a sampling error, that is, uncertainty of radar observations (e.g., Kim et al. 2008; Lipa et al. 2006). A pair of radial velocities (r_A and r_B) reported from sites A and B is given as

$$r_A = u \cos \theta_A + v \sin \theta_A + \varepsilon_A, \quad (13)$$

$$r_B = u \cos \theta_B + v \sin \theta_B + \varepsilon_B, \quad (14)$$

where θ_{ij} denotes the bearing angles at individual radar sites and ε indicates a sampling error.

The standard deviation (λ) of the sum of a paired radial time series is formulated as a function of the difference between bearing angles (δ ; $\delta = \theta_A - \theta_B$):

$$\lambda = \sqrt{\langle (r_A + r_B)^2 \rangle} = \sqrt{4\sigma^2 \cos^2 \frac{\delta}{2} + 2\gamma^2}, \quad (15)$$

where the current field is assumed to be isotropic—that is, the variance of the vector components and their error variance in the x and y directions are identical, respectively.

$$\langle u^2 \rangle = \langle v^2 \rangle = \sigma^2 \quad \text{and} \quad \langle \varepsilon_A^2 \rangle = \langle \varepsilon_B^2 \rangle = \gamma^2, \quad (16)$$

respectively—and $\sqrt{2}\gamma$ is the error of a sum of oppositely directed radial velocities ($\delta = \pm\pi$).

Similarly, the cross correlation (ρ) between paired radials is given as

$$\rho = \frac{\langle r_A r_B^\dagger \rangle}{\sqrt{\langle r_A^2 \rangle} \sqrt{\langle r_B^2 \rangle}} = \kappa \cos \delta, \quad (17)$$

where the dagger (†) denotes the vector transpose and $\kappa = \sigma^2/(\sigma^2 + \gamma^2)$.

The nearest distance [d in Eq. (19)] between data (δ, ρ) and a cost function [Eq. (17)] is quantified [Eq. (19)], and its ensemble mean is defined as the deviation (ξ) of the correlation of paired radials, which describes the degree of spatial consistency based on the radial observations themselves:

$$\xi = \langle d \rangle, \quad (18)$$

where

$$d = d(\delta_0) = \frac{|\kappa(\delta - \delta_0) \sin \delta_0 + \rho - \kappa \cos \delta_0|}{\sqrt{\kappa^2 \sin^2 \delta_0 + 1}}. \quad (19)$$

Instead of finding an analytic solution to Eq. (19), a local and unique solution (δ_0 ; $|\delta - \delta_0| \leq 5^\circ$) that minimizes the distance [d in Eq. (19)] can be found.

Additionally, the SNR (χ) of radial velocity data in a coastal region is defined as

$$\chi = \frac{\sigma^2}{\gamma^2} = \frac{\rho}{\cos \delta - \rho}. \quad (20)$$

When radials face opposite directions and are perfectly matched—that is, $\delta = \pm\pi$ and $\rho = -1$ —the SNR becomes ∞ . When the radials are facing the same direction and are perfectly matched—that is, $\delta = 0$ or 2π and $\rho = 1$ —the SNR becomes ∞ .

As a strict criterion for an uncertainty estimate, an area of polar grid patches in two different radar sites can be considered. Since a radar frequency (e.g., operating and sweeping frequencies) is closely related to the area of the polar grid patch, radials derived from radars with a similar order of frequency or radials reported at the radar grid to have a similar order of azimuthal spacing and range spacing are taken into account. However, under this criterion, the paired radials may not be found with sufficient realizations. Thus, in this paper, the paired radials were chosen when they are within a threshold distance (e.g., 200 m) between two radial grid points, defined from different radars.

The uncertainty of radar observations off Yeosu Bay is reported as 6.1 cm s^{-1} for the 25-MHz system (Fig. 9a) and 12.6 cm s^{-1} for the 44-MHz system (not shown) based on paired radials obtained from NAM4, HYIL, NHSP, and ODNG (Yeosu Bay) over a period of 2 years (2007–08). The SNR of the 25-MHz system is approximately 4.5 (Fig. 9b). The deviation of the correlation of paired radials obtained from the 25-MHz system is estimated as 0.217. The 44-MHz system has been deployed in a channel, and a high noise level might be caused by interference from the land.

Uncertainty estimates using independent in situ observations have been addressed elsewhere (e.g., Emery et al. 2004; Kaplan et al. 2005; Liu et al. 2010; Paduan et al. 2006). Additionally, the sampling depth, sampling area, and type of signals (e.g., geostrophic or ageostrophic currents) should be taken into account to accurately quantify the uncertainty.

f. Consistency related to antenna patterns

The standard deviation (ζ) of the difference of radial velocities estimated from ideal (r^I) and measured (r^M) beam patterns is defined as

$$\zeta(m, \theta) = \sqrt{\langle |r^I(m, \theta) - r^M(m, \theta)|^2 \rangle}. \quad (21)$$

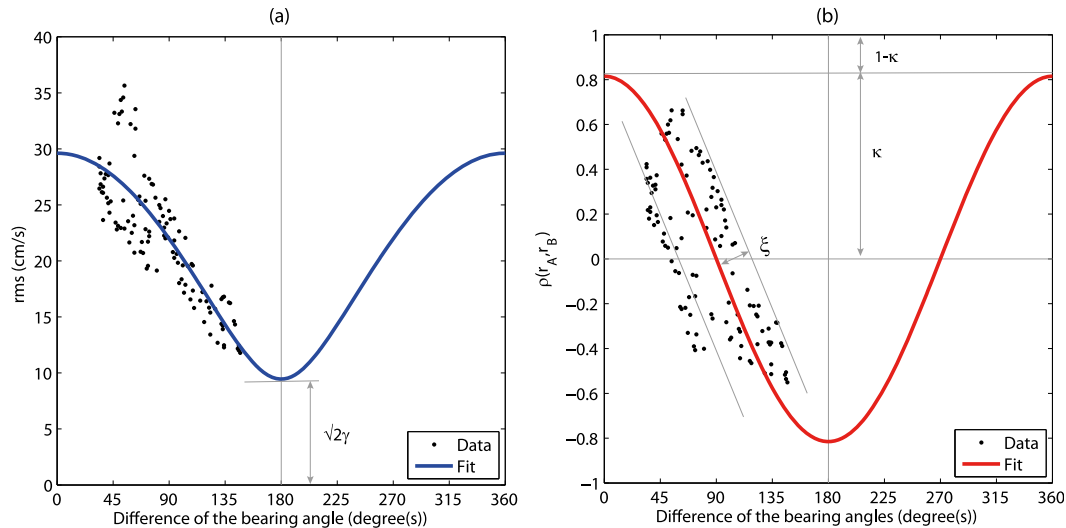


FIG. 9. (a) Standard deviation [λ ; Eq. (15)] and (b) cross correlation [ρ ; Eq. (17)] of paired radial time series at NAM4 and HYIL (Yeosu Bay). Paired time series are obtained from 5° spacing radial velocity maps with more than concurrent 50% spatial data availability. The deviation of the correlation [ξ ; Eq. (18)] is 0.217 and the estimated SNR [χ ; Eq. (20)] is 4.5.

Although radial velocities derived from two radar beam patterns (e.g., ideal and measured beam patterns) may be different from the true current field, the statistics of their difference can be used as a tool to identify spatial sensitivity, including spatial bias and distortions in radial velocity maps (Fig. 10). The radials at the 287° azimuthal bin appear spurious due to a distorted measured beam pattern at that azimuthal bin, which is visible in Figs. 7b and 7e as well.

4. Summary

This technical paper summarizes several ways to conduct quality assessment of the archived surface radial

velocities observed from shore-based single or multiple high-frequency radars. As a single radial velocity map contains geophysical signals, their energy spectra exhibit variance associated with surface tides, wind stress, and near-inertial and low-frequency signals. The spatial consistency of radial velocity maps allows us to identify a spurious range and azimuthal bin. In particular, spatial coherence within a frequency band—that is, maps of the amplitude and phase at primary tidal constituents (e.g., harmonic analysis), and wind-radial velocity transfer function analysis—are suggested. The uncertainty of the radar observation itself can be estimated with paired radials obtained at nearby grid points and from two different

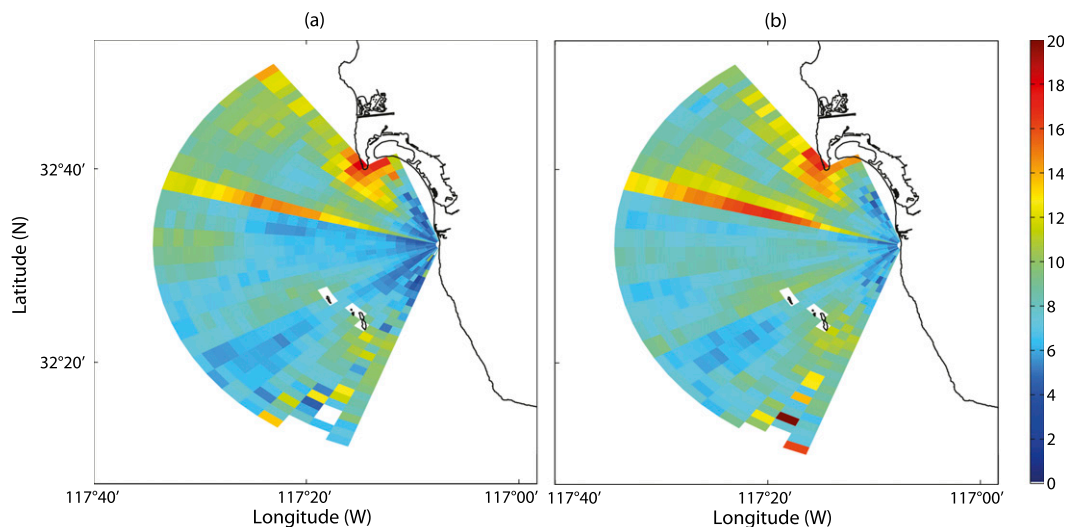


FIG. 10. Standard deviation [ζ in Eq. (21); cm s^{-1}] of the difference between hourly radial velocities estimated from ideal and measured beam patterns at SDBP for a period of one month for (a) September 2003 and (b) October 2003.

radar sites. This review paper can be useful to evaluate and to analyze radial velocity data as a part of quality assurance and quality control using statistical and dynamical approaches. Although the examples reported in this technical review are based on radials obtained from a compact array system, the statistical and dynamical analyses presented here can be applicable to the radials observed with a phase array system as well.

As the fundamental data in between spectral raw data (e.g., Kirincich et al. 2012; Flores-Vidal et al. 2013) and vector current maps (e.g., Kim et al. 2008) derived from HFRs, the radial velocity data on polar coordinates contain geophysical signals and corresponding unique spatial structures. The QAQC of radial velocity data is essential for improving the quality of vector current maps and addressing coastal circulation studies along with numerical models (e.g., data assimilation). This review paper clarifies how to analyze HFR-derived radial velocity data and complex geophysical data.

As the proposed techniques require archived data over a time period of at least one year, they may have a limitation with respect to a quick assessment. However, evaluating the periodicity in the radial data and spatial patterns requires multiple realizations to ensure statistical confidence, which leads to reliable determination of spurious data and areas.

Acknowledgments. Sung Yong Kim is supported by the Basic Science Research Program through the National Research Foundation (NRF), Ministry of Education (NRF-2013R1A1A2057849), and by the Human Resources Development of the Korea Institute of Energy Technology Evaluation and Planning (KETEP), Ministry of Trade, Industry and Energy (20114030200040), South Korea. Surface currents data are provided by Scripps Institution of Oceanography (SIO) at University of California, San Diego; California Polytechnic State University (CalPoly); Oregon State University (OSU; Kim et al. 2011); and the Korea Hydrographic and Oceanographic Administration (KHOA). Wind data are from the National Data Buoy Center (NDBC).

REFERENCES

- Barrick, D. E., M. W. Evans, and B. L. Weber, 1977: Ocean surface currents mapped by radar. *Science*, **198**, 138–144, doi:10.1126/science.198.4313.138.
- Bjorkstedt, E., and Coauthors, 2010: State of the California Current 2009–2010: Regional variation persists through transition from La Niña to El Niño (and back?). California Cooperative Oceanic Fisheries Investigations reports, J. N. Heine, Ed., Vol. 51, CalCOFI, 39–69.
- Chavanne, C., P. Flament, G. Carter, M. Merrifield, D. Luther, E. D. Zaron, and K.-W. Gurgel, 2010a: The surface expression of semidiurnal internal tides near a strong source at Hawaii. Part I: Observations and numerical predictions. *J. Phys. Oceanogr.*, **40**, 1155–1179, doi:10.1175/2010JPO4222.1.
- , —, P. Klein, and K.-W. Gurgel, 2010b: Interactions between a submesoscale anticyclonic vortex and a front. *J. Phys. Oceanogr.*, **40**, 1802–1818, doi:10.1175/2010JPO4055.1.
- Crombie, D. D., 1955: Doppler spectrum of sea echo at 13.56 Mc/s. *Nature*, **175**, 681–682, doi:10.1038/175681a0.
- Dickey, T., M. Lewis, and G. Chang, 2006: Optical oceanography: Recent advances and future directions using global remote sensing and in situ observations. *Rev. Geophys.*, **44**, RG1001, doi:10.1029/2003RG000148.
- Emery, B. M., L. Washburn, and J. Harlan, 2004: Evaluating radial current measurements from CODAR high-frequency radars with moored current meters. *J. Atmos. Oceanic Technol.*, **21**, 1259–1271, doi:10.1175/1520-0426(2004)021<1259:ERCMEFC>2.0.CO;2.
- Emery, W. J., and R. E. Thomson, 1997: *Data Analysis Methods in Physical Oceanography*. Elsevier, 634 pp.
- Essen, H.-H., K.-W. Gurgel, and T. Schlick, 1999: Measurement of ocean wave height and direction by means of HF radar: An empirical approach. *Dtsch. Hydrogr. Z.*, **51**, 369–383, doi:10.1007/BF02764161.
- Flores-Vidal, X., P. Flament, R. Durazo, C. Chavanne, and K.-W. Gurgel, 2013: High-frequency radars: Beamforming calibrations using ships as reflectors. *J. Atmos. Oceanic Technol.*, **30**, 638–648, doi:10.1175/JTECH-D-12-00105.1.
- Fu, L.-L., and R. Ferrari, 2008: Observing oceanic submesoscale processes from space. *Eos, Trans. Amer. Geophys. Union*, **89**, 488–488, doi:10.1029/2008EO480003.
- Gonella, J., 1972: A rotary-component method for analysis in meteorological and oceanographic vector time series. *Deep-Sea Res. Oceanogr. Abstr.*, **19**, 833–846, doi:10.1016/0011-7471(72)90002-2.
- Gough, M. K., N. Garfield, and E. McPhee-Shaw, 2010: An analysis of HF radar measured surface currents to determine tidal, wind-forced and seasonal circulation in the Gulf of the Farallones, California, United States. *J. Geophys. Res.*, **15**, C04019, doi:10.1029/2009JC005644.
- Johnson, D. R., 2008: Ocean surface current climatology in the northern Gulf of Mexico. University of Southern Mississippi, Gulf Coast Research Laboratory Tech. Rep., 37 pp.
- Kaplan, D. M., and J. L. Largier, 2006: HF radar-derived origin and destination of surface waters off Bodega Bay, California. *Deep-Sea Res. II*, **53**, 2906–2930, doi:10.1016/j.dsr2.2006.07.012.
- , —, and L. W. Botsford, 2005: HF radar observations of surface circulation off Bodega Bay (northern California, USA). *J. Geophys. Res.*, **110**, C10020, doi:10.1029/2005JC002959.
- Kim, S. Y., 2010: Observations of submesoscale eddies using high-frequency radar-derived kinematic and dynamic quantities. *Cont. Shelf Res.*, **30**, 1639–1655, doi:10.1016/j.csr.2010.06.011.
- , and P. M. Kosro, 2013: Observations of near-inertial surface currents off Oregon: Decorrelation time and length scales. *J. Geophys. Res. Oceans*, **118**, 3723–3736, doi:10.1002/jgrc.20235.
- , E. J. Terrill, and B. D. Cornuelle, 2008: Mapping surface currents from HF radar radial velocity measurements using optimal interpolation. *J. Geophys. Res.*, **113**, C10023, doi:10.1029/2007JC004244.
- , B. D. Cornuelle, and E. J. Terrill, 2009a: Anisotropic response of surface currents to the wind in a coastal region. *J. Phys. Oceanogr.*, **39**, 1512–1533, doi:10.1175/2009JPO4013.1.
- , E. J. Terrill, and B. D. Cornuelle, 2009b: Assessing coastal plumes in a region of multiple discharges: The U.S.–Mexico border. *Environ. Sci. Technol.*, **43**, 7450–7457, doi:10.1021/es900775p.

- , B. D. Cornuelle, and E. J. Terrill, 2010a: Decomposing observations of high-frequency radar-derived surface currents by their forcing mechanisms: Decomposition techniques and spatial structures of decomposed surface currents. *J. Geophys. Res.*, **115**, C12007, doi:[10.1029/2010JC006222](https://doi.org/10.1029/2010JC006222).
- , —, and —, 2010b: Decomposing observations of high-frequency radar-derived surface currents by their forcing mechanisms: Locally wind-driven surface currents. *J. Geophys. Res.*, **115**, C12046, doi:[10.1029/2010JC006223](https://doi.org/10.1029/2010JC006223).
- , and Coauthors, 2011: Mapping the U.S. West Coast surface circulation: A multiyear analysis of high-frequency radar observations. *J. Geophys. Res.*, **116**, C03011, doi:[10.1029/2010JC006669](https://doi.org/10.1029/2010JC006669).
- , G. Gopalakrishnan, and A. Ponte, 2015: Interpretation of coastal wind transfer functions with momentum balances derived from idealized numerical model simulations. *Ocean Dyn.*, **65**, 115–141, doi:[10.1007/s10236-014-0766-x](https://doi.org/10.1007/s10236-014-0766-x).
- Kirincich, A. R., T. De Paolo, and E. Terrill, 2012: Improving HF radar estimates of surface currents using signal quality metrics, with application to the MVCO high-resolution radar system. *J. Atmos. Oceanic Technol.*, **29**, 1377–1390, doi:[10.1175/JTECH-D-11-00160.1](https://doi.org/10.1175/JTECH-D-11-00160.1).
- Kurapov, A. L., G. D. Egbert, J. S. Allen, R. N. Miller, S. Y. Erofeeva, and P. M. Kosro, 2003: The M_2 internal tide off Oregon: Inference from data assimilation. *J. Phys. Oceanogr.*, **33**, 1733–1757, doi:[10.1175/2397.1](https://doi.org/10.1175/2397.1).
- Lipa, B. J., and D. E. Barrick, 1983: Least-squares methods for the extraction of surface currents from CODAR crossed-loop data: Application at ARSLOE. *IEEE J. Oceanic Eng.*, **8**, 226–253, doi:[10.1109/JOE.1983.1145578](https://doi.org/10.1109/JOE.1983.1145578).
- , B. Nyden, D. S. Ullman, and E. Terrill, 2006: SeaSonde radial velocities: Derivation and internal consistency. *IEEE J. Oceanic Eng.*, **31**, 850–861, doi:[10.1109/JOE.2006.886104](https://doi.org/10.1109/JOE.2006.886104).
- Liu, Y., R. H. Weisberg, C. R. Merz, S. Lichtenwalner, and G. J. Kirkpatrick, 2010: HF radar performance in a low-energy environment: CODAR SeaSonde experience on the West Florida shelf. *J. Atmos. Oceanic Technol.*, **27**, 1689–1710, doi:[10.1175/2010JTECH0720.1](https://doi.org/10.1175/2010JTECH0720.1).
- Malone, T. C., and M. Cole, 2000: Toward a global scale coastal ocean observing system. *Oceanography*, **13**, 7–11, doi:[10.5670/oceanog.2000.48](https://doi.org/10.5670/oceanog.2000.48).
- Mao, Y., and M. L. Heron, 2008: The influence of fetch on the response of surface currents to wind studied by HF ocean surface radar. *J. Phys. Oceanogr.*, **38**, 1107–1121, doi:[10.1175/2007JPO3709.1](https://doi.org/10.1175/2007JPO3709.1).
- Ocean. US, 2002: An Integrated and Sustained Ocean Observing System (IOOS) for the United States: Design and implementation. Tech. Rep., 21 pp.
- Paduan, J. D., and M. S. Cook, 1997: Mapping surface currents in Monterey Bay with CODAR-type HF radar. *Oceanography*, **10**, 49–52.
- , and L. Washburn, 2013: High-frequency radar observations of ocean surface currents. *Annu. Rev. Mar. Sci.*, **5**, 115–136, doi:[10.1146/annurev-marine-121211-172315](https://doi.org/10.1146/annurev-marine-121211-172315).
- , K. C. Kim, M. S. Cook, and F. P. Chavez, 2006: Calibration and validation of direction-finding high-frequency radar ocean surface current observations. *IEEE J. Oceanic Eng.*, **31**, 862–875, doi:[10.1109/JOE.2006.886195](https://doi.org/10.1109/JOE.2006.886195).
- Picaut, J., A. J. Busalacchi, M. J. McPhaden, and B. Camusat, 1990: Validation of the geostrophic method for estimating zonal currents at the equator from Geosat altimeter data. *J. Geophys. Res.*, **95**, 3015–3024, doi:[10.1029/JC095iC03p03015](https://doi.org/10.1029/JC095iC03p03015).
- Rogowski, P. A., E. Terrill, K. Schiff, and S. Y. Kim, 2015: An assessment of the transport of southern California stormwater ocean discharges. *Mar. Pollut. Bull.*, **90**, 135–142, doi:[10.1016/j.marpolbul.2014.11.004](https://doi.org/10.1016/j.marpolbul.2014.11.004).
- Rosenfeld, L., I. Shulman, M. Cook, J. Paduan, and L. Shulman, 2009: Methodology for a regional tidal model evaluation, with application to central California. *Deep-Sea Res. II*, **56**, 199–218, doi:[10.1016/j.dsr2.2008.08.007](https://doi.org/10.1016/j.dsr2.2008.08.007).
- Schmidt, R. O., 1986: Multiple emitter location and signal parameter estimation. *IEEE Trans. Antennas Propag.*, **34**, 276–280, doi:[10.1109/TAP.1986.1143830](https://doi.org/10.1109/TAP.1986.1143830).
- Shay, L. K., H. C. Graber, D. B. Ross, and R. D. Chapman, 1995: Mesoscale ocean surface current structure detected by high-frequency radar. *J. Atmos. Oceanic Technol.*, **12**, 881–900, doi:[10.1175/1520-0426\(1995\)012<0881:MOSCSO>2.0.CO;2](https://doi.org/10.1175/1520-0426(1995)012<0881:MOSCSO>2.0.CO;2).
- , T. N. Lee, E. J. Williams, H. C. Graber, and C. G. H. Rooth, 1998: Effects of low-frequency current variability on near-inertial submesoscale vortices. *J. Geophys. Res.*, **103**, 18 691–18 714, doi:[10.1029/98JC01007](https://doi.org/10.1029/98JC01007).
- Stewart, R. H., and J. W. Joy, 1974: HF radio measurements of surface currents. *Deep-Sea Res. Oceanogr. Abstr.*, **21**, 1039–1049, doi:[10.1016/0011-7471\(74\)90066-7](https://doi.org/10.1016/0011-7471(74)90066-7).
- Stokstad, E., 2006: Senate panel backs Integrated Ocean Observation System. *Science*, **313**, 280, doi:[10.1126/science.313.5785.280a](https://doi.org/10.1126/science.313.5785.280a).
- Teague, C. C., J. F. Vesecky, and Z. R. Hallock, 2001: A comparison of multifrequency HF radar and ADCP measurements of near-surface currents during COPE-3. *IEEE J. Oceanic Eng.*, **26**, 399–405, doi:[10.1109/48.946513](https://doi.org/10.1109/48.946513).
- Uematsu, A., R. Nakamura, Y. Nakajima, and Y. Yajima, 2013: X-band interferometric SAR sensor for the Japanese altimetry mission, COMPIRA. *2013 IEEE International Geoscience and Remote Sensing Symposium: Proceedings*, IEEE, 2943–2946.
- Ullman, D. S., J. O'Donnell, J. Kohut, T. Fake, and A. Allen, 2006: Trajectory prediction using HF radar surface currents: Monte Carlo simulations of prediction uncertainties. *J. Geophys. Res.*, **111**, C12005, doi:[10.1029/2006JC003715](https://doi.org/10.1029/2006JC003715).
- Zaron, E., C. Chavanne, G. Egbert, and P. Flament, 2009: Baroclinic tidal generation in the Kauai Channel inferred from high-frequency radar Doppler currents. *Dyn. Atmos. Oceans*, **48**, 93–120, doi:[10.1016/j.dynatmoce.2009.03.002](https://doi.org/10.1016/j.dynatmoce.2009.03.002).